

NEUROSCIENCE

Ring attractor dynamics in the *Drosophila* central brain

Sung Soo Kim,* Hervé Rouault,* Shaul Druckmann,† Vivek Jayaraman†

Ring attractors are a class of recurrent networks hypothesized to underlie the representation of heading direction. Such network structures, schematized as a ring of neurons whose connectivity depends on their heading preferences, can sustain a bump-like activity pattern whose location can be updated by continuous shifts along either turn direction. We recently reported that a population of fly neurons represents the animal's heading via bump-like activity dynamics. We combined two-photon calcium imaging in head-fixed flying flies with optogenetics to overwrite the existing population representation with an artificial one, which was then maintained by the circuit with naturalistic dynamics. A network with local excitation and global inhibition enforces this unique and persistent heading representation. Ring attractor networks have long been invoked in theoretical work; our study provides physiological evidence of their existence and functional architecture.

Studies of neural circuits near the sensory periphery have produced deep mechanistic insights into circuit functions (1, 2). However, it has been more challenging to understand circuit functions in central brain regions dominated by recurrent networks, which often produce complex neural activity patterns. These dynamics play a major role in shaping cognitive functions (3–7), such as the maintenance of heading information during navigation (8–10). A heading representation must be unique (because an animal can face only one direction at a given time) and persistent (to allow an animal to keep its bearings in darkness), yet must allow updating that matches the magnitude and speed of heading changes expected from the animal's movements. Theoretically, this can be accomplished by ring attractor networks (11–14), wherein the position of a localized subset of active neurons in a topological ring represents the animal's heading direction. However, whether the brain uses these hypothesized networks is still unknown (8, 15). A recent study reported that a population of neurons, called E-PG neurons (Fig. 1, C and D; see supplementary materials for nomenclature), in the *Drosophila melanogaster* ellipsoid body (EB) appears to use bump-like neural activity dynamics to represent the animal's heading in visual environments and in darkness (16, 17). Here, we establish essential properties of the network that enables this representation.

We first determined whether the E-PG population activity bump tracks the fly's heading direction relative to its visual surroundings during tethered flight (Fig. 1 and fig. S1). We used two-photon imaging with the genetically encoded calcium indicator GCaMP6f (18) to record dendritic calcium activity of the entire E-PG population in the EB while the fly was flying in a virtual-reality LED arena. The azimuthal velocity of the visual

scene was proportional to the fly's yaw velocity (Fig. 1, A and B). As with walking flies (16), E-PG population activity during flight was organized into a single bump, whether the visual scene contained a single bar (fig. S1B) or a more complex pattern (Fig. 1G). The activity bump closely tracked the fly's heading in flight (Fig. 1K) and persisted in darkness (Fig. 1H). However, unlike in walking, the activity bump seldom tracked the fly's motor actions in darkness (Fig. 1, H and K, and fig. S1C), potentially because tethering deprives the fly of normal sensory feedback about its rotational movements from its halteres (19). Although the location of the activity bump eventually drifted in some flies, the bump's movement was, on average, uncorrelated to the animal's turning movements in darkness (Fig. 1K). These findings suggest that the representation of heading in the E-PG population has intact, visually driven dynamics as well as persistence, but is largely uncoupled from updating by self-motion cues during tethered flight.

To test whether the fly's compass network enforces a unique bump within the EB, we took advantage of the relative persistence of the visually evoked activity bump in darkness, and asked whether this bump could coexist with an "artificial" bump of activity. We used localized optogenetic stimulation to create artificial activity bumps in different locations within the E-PG population. Using a transgenic fly line in which E-PG neurons co-expressed CsChrimson (20) and GCaMP6f, we used alternating two-photon laser scan lines of excitation (higher laser intensity) and imaging (normal laser intensity) to monitor changes in E-PG population dynamics in response to an optogenetically created spot of local activity (Fig. 2, A and B, and fig. S2, A and B). By varying the intensity of stimulation light delivered to the target location, we could create bumps of increased calcium activity (Fig. 2, C to F, and movie S1). As the new bump formed, activity at the previous location began to decline and eventually disappeared (Fig. 2D) without significantly perturbing the fly's behavior (but see fig. S2E). When the optogenetic excitation

was terminated, the amplitude of the artificially created bump settled at levels typically evoked by sensory stimuli and did not disappear; it either stayed in the induced location for several seconds (fig. S2F) or slowly drifted away (see below) (Fig. 3).

The bump's uniqueness may arise through either recurrent mutual suppression or an indirect mechanism whereby strong bump activity in the EB functionally inhibits feedforward sensory inputs to other E-PG neurons. To discriminate between these alternatives, we simultaneously excited two locations on the EB ring. A reference location was excited at a fixed laser power, and a second, spatially offset location was excited at increasing levels of laser power (fig. S2G and movies S3 to S5). We could always suppress the reference bump by increasing laser power at the second location above a certain threshold, consistent with mutual suppression.

Recurrent suppression can ensure a unique activity bump through a simple winner-take-all (WTA) circuit (fig. S3A). However, an animal's representation of its angular orientation should favor more continuous updates based on turning actions. Such gradual, ordered drift to nearby locations would be more consistent with continuous, or ring, attractor models (fig. S3, B to D). We therefore examined changes in the location of an artificially created bump after the stabilization of its peak activity at the "natural" level. The experiments were performed in darkness to untether the bump from any potentially lingering visual input (Fig. 3). If EB dynamics were driven by a WTA network, bumps would be expected to disappear at times and to jump to random distant locations (fig. S3E). In contrast, the bump drifted gradually around the EB (Fig. 3, B and D, and movie S6); this finding suggests that the fly's heading representation is updated through functionally excitatory interactions between neighboring E-PG neurons, consistent with a ring attractor model. These observations together rule out the possibility that network dynamics in darkness result purely from cell-intrinsic mechanisms (21, 22) or slowly decaying visual input. Most important, direct manipulation of E-PG neuron activity changed the network state, which implies that E-PG neurons do not merely mirror dynamics occurring in a different circuit, but are themselves an important component of the ring attractor (23).

We next aimed to dissect the effective connectivity pattern underlying ring attractor dynamics in the E-PG population. A wide range of network structures can, in principle, implement ring attractors (11, 13, 14, 24, 25). We focused our efforts to a model space between two extreme network architectures that are analytically solvable: (i) a "global model" based on global cosine-shaped interactions (fig. S3B) (11, 13, 26) and (ii) a "local model" based on relatively local excitatory interactions (fig. S3D and supplementary text) (24, 27). Under constraints of a fixed bump width of 90° to match physiological observations (Fig. 1J) and an assumption of effectively excitatory visual input without any negative bias, both models could

Howard Hughes Medical Institute, Janelia Research Campus, Ashburn, VA 20147, USA.

*These authors contributed equally to this work.

†Corresponding author. Email: druckmanns@janelia.hhmi.org (S.D.); vivek@janelia.hhmi.org (V.J.)

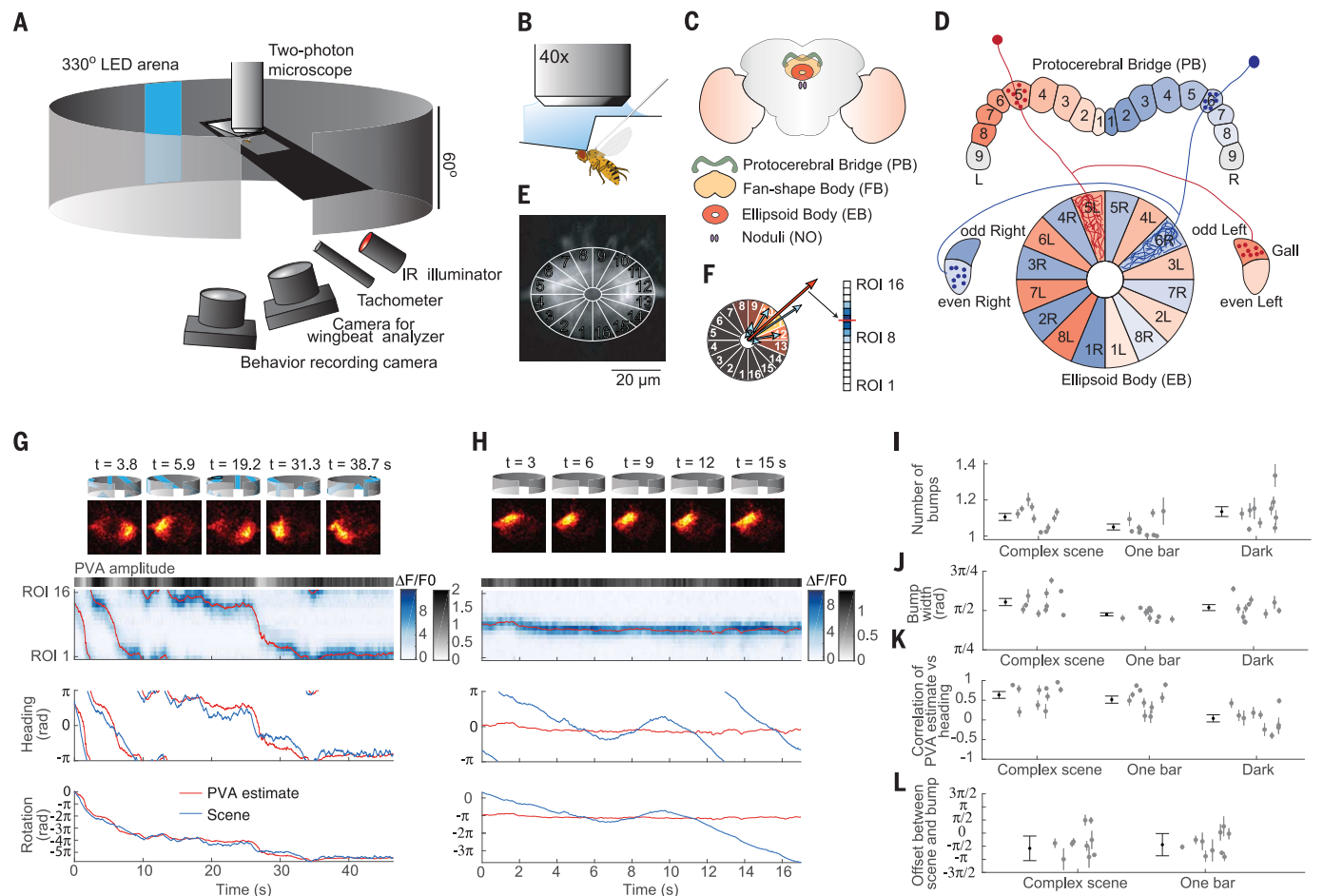


Fig. 1. E-PG neurons encode body orientation relative to the visual world during tethered closed-loop flight. (A) Setup schematic. (B) Close-up of tethered flying fly. (C) Central complex. (D) Dendrites of each E-PG neuron innervate wedge-shaped segment of EB; axons project to corresponding glomeruli in PB and Gall. (E) Averaged calcium image of dendritic processes of entire E-PG population segmented into 16 regions of interest (ROIs). (F) Position (PVA direction) and strength (PVA amplitude) of bump obtained by summation of 16 vectors whose lengths represent magnitude of fluorescence transients ($\Delta F/F_0$). (G) GCaMP6f fluorescence transients in E-PG dendrites during tethered flight in complex visual scene. Top: Visual pattern at sample

time points. Second row: Sample frames of calcium imaging. Third row: $\Delta F/F_0$ of 16 ROIs. Grayscale band denotes PVA amplitude; red line is PVA estimate. Fourth row: PVA estimate and heading (blue). Bottom: Same as fourth row, but unwrapped. (H) Fluorescence transients in darkness. (I) Number of activity bumps in E-PG population across flies ($n = 10$) for three visual conditions. Each dot with vertical line indicates mean \pm SEM for each fly. Population mean \pm SEM is shown at left of each scatterplot. (J) Bump width measured by full width at half maximum. (K) Correlation between estimated bump position and heading. (L) Angular offset between PVA estimate and scene orientation. Whisker plots, mean \pm circular SD.

explain the basic properties of bump dynamics, including its uniqueness and its persistence in darkness. We therefore probed the network's response to more artificial conditions, such as abrupt visual stimulus shifts.

We first examined experimentally how the E-PG population responded to unnatural, abrupt visual shifts. Depending on the distance of the shift, the E-PG bump either “flowed” continuously (shorter shift distances; Fig. 4, A and C, and movies S7 and S8) or “jumped” to the new location (longer shift distances; Fig. 4, B and D, and movie S9) (16). In simulations, both models predicted a mixture of jump and flow responses, depending on the strength and width of the abruptly shifting visual input (Fig. 4D, fig. S4A, and supplementary text). For example, weak wide input induced flows and strong narrow input evoked jumps (Fig. 4D). However, the jump-flow balance predicted by the two

models differed and was more consistent with the local model in several aspects (Fig. 4D and fig. S4A). First, the visual input strength we inferred from normal conditions was much weaker than required by the global model for bump jumps (fig. S1D). Second, the global model required a much-wider-than-normal range of visual input strengths to explain jumps at multiple distances (Fig. 4D, fig. S1D, and fig. S4A). Third, using parameters consistent with the rest of our findings, we could reproduce the jump-flow ratio observed in Fig. 4C with the local model but not with the global model (fig. S4B).

To obtain more concrete evidence, we compared model predictions to experimentally observed bump dynamics, under conditions in which input strength, polarity, and shift distance were controlled through optogenetic stimulation. To simulate moderate and large input shift distances, we se-

quentially stimulated two small regions in the EB—each with an angular width of 22.5° —separated by either 90° or 180° (Fig. 4, E to G, movie S10, and fig. S4, C to E). We then varied the stimulation laser power to detect the threshold required for the bump to jump (Fig. 4E). The laser power required to elicit a jump was not significantly different between the two different shift distances, favoring the local model (Fig. 4F). We then inferred the strength of input to the network by comparing the amplitude of the optogenetically evoked bump to natural bump amplitudes in darkness. The optogenetic input strength required to induce jumps was smaller than the global model's prediction but matched that of the local model (Fig. 4G) and the range of the inferred visual input strength under normal conditions (fig. S1D, fig. S4, D and E, and movie S11). Finally, when we tested intermediate models that lie between the extremes of

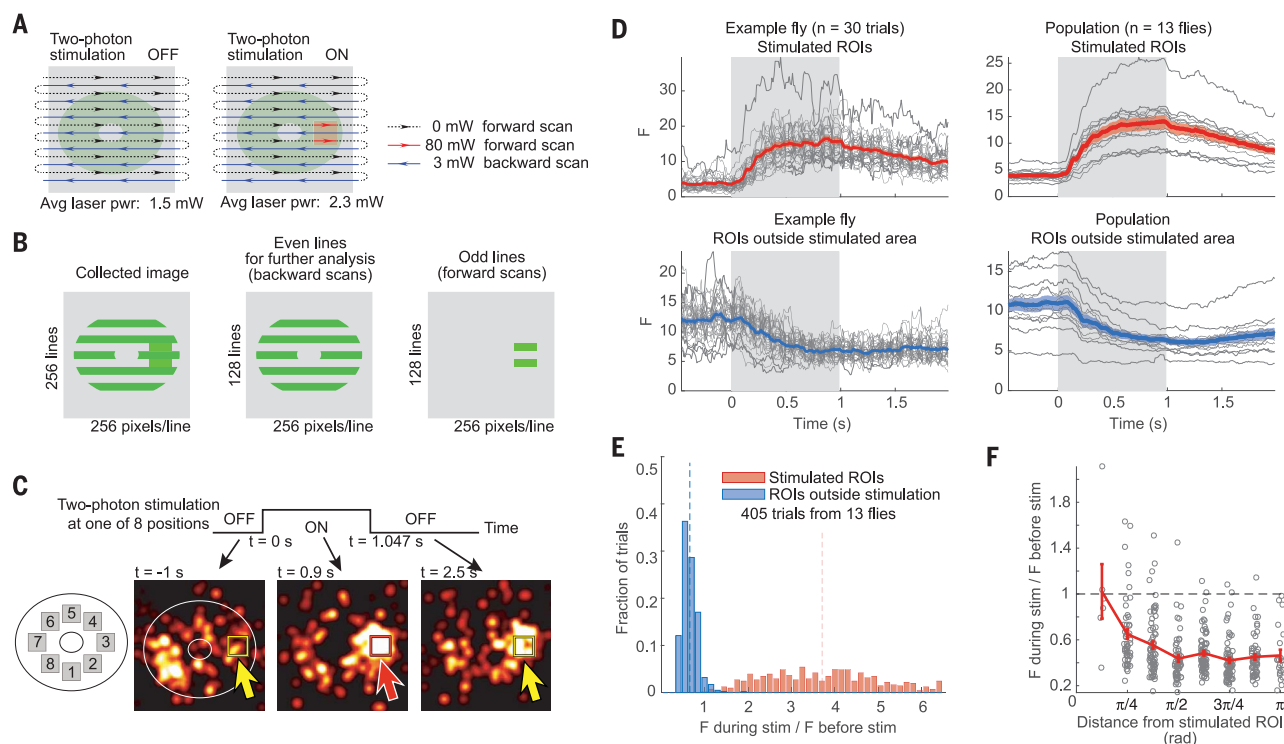


Fig. 2. E-PG neurons compete by mutually suppressing each other through recurrent connections. (A) Schematic of simultaneous calcium imaging and localized optogenetic stimulation. (B) Analysis procedure for collected images. (C) Top: Temporal profile of two-photon optogenetic stimulation. Bottom: Three sample frames (smoothed with Gaussian filter). Yellow rectangle with arrow, stimulus OFF; red rectangle with arrow, stimulus ON. (D) Time course of calcium dynamics from example fly (left) and population (right). Gray background, optogenetic stimulation period; gray lines, individual trials (left) or flies (right). Top: Mean F of stimulated

ROIs. Bottom: Mean of the four most active ROIs outside optogenetically stimulated area before stimulation. Thick colored lines and colored shaded area denote mean and SEM, respectively. (See fig. S2C for control experiment.) (E) Distribution of fluorescence ratio during and before stimulation. $P < 0.001$, Wilcoxon rank sum test between stimulated (red) and outside stimulation (blue) areas. (See fig. S2D for control experiment.) (F) Suppression by optogenetic stimulation. The x axis indicates distance from stimulation position to existing bump; $P < 0.001$, t test for each distance. Limited sample size prevented a statistical test for $\pi/8$.

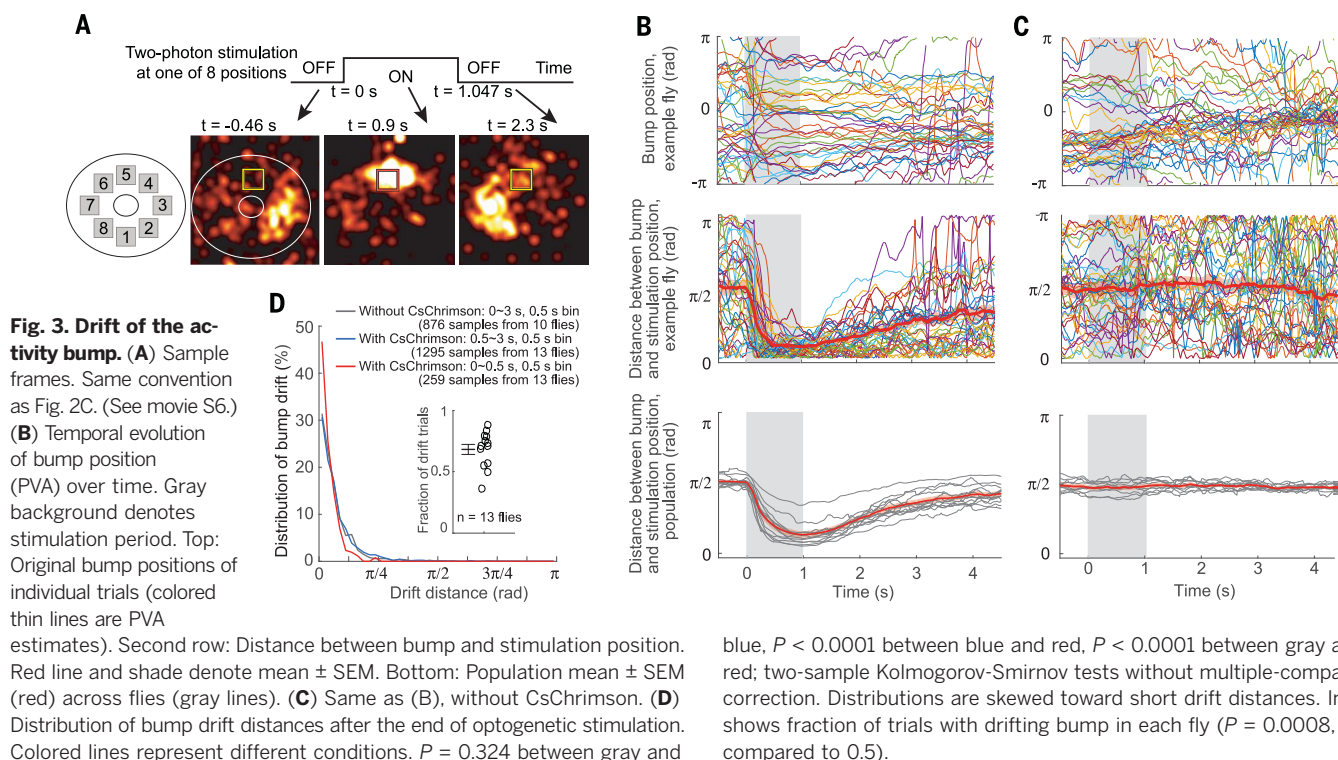


Fig. 3. Drift of the activity bump. (A) Sample frames. Same convention as Fig. 2C. (See movie S6.) (B) Temporal evolution of bump position (PVA) over time. Gray background denotes stimulation period. Top: Original bump positions of individual trials (colored thin lines are PVA estimates). Second row: Distance between bump and stimulation position. Red line and shade denote mean \pm SEM. Bottom: Population mean \pm SEM (red) across flies (gray lines). (C) Same as (B), without CsChrimson. (D) Distribution of bump drift distances after the end of optogenetic stimulation. Colored lines represent different conditions. $P = 0.324$ between gray and

blue, $P < 0.0001$ between blue and red, $P < 0.0001$ between gray and red; two-sample Kolmogorov-Smirnov tests without multiple-comparisons correction. Distributions are skewed toward short drift distances. Inset shows fraction of trials with drifting bump in each fly ($P = 0.0008$, t test compared to 0.5).

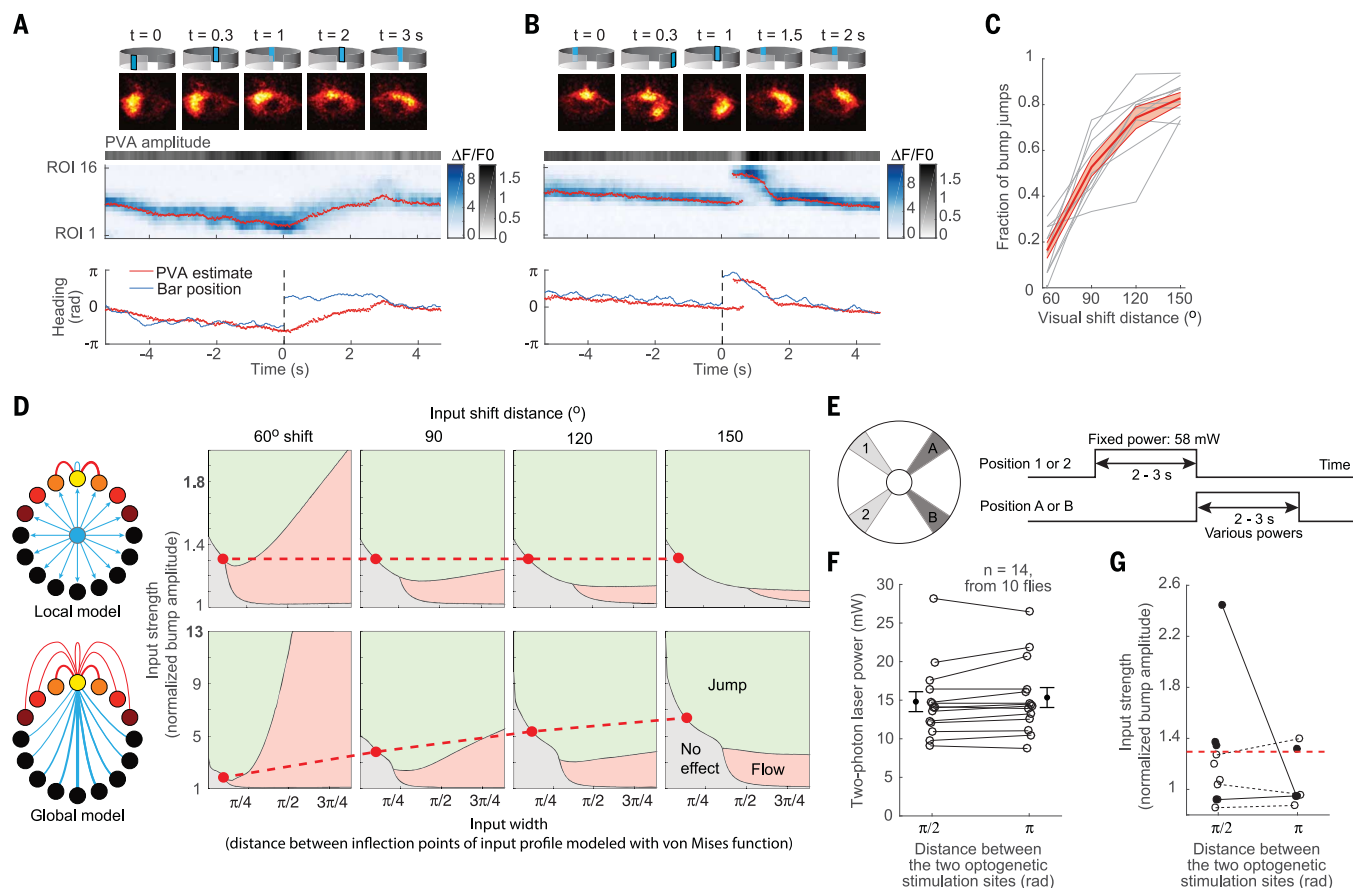


Fig. 4. Probing the connectivity profile of the ring attractor network.

(A) Example of bump “flow” in response to abrupt shift of vertical bar. Same convention as Fig. 1G. Red dots are bump positions estimated from Bayesian sampling method. (B) Bump “jump.” (C) Jump probability increases with distance of visual input shift. Red line and shading denote mean \pm SEM. (D) Input-response phase diagrams. Top: Response of local model (fig. S3D) to various input widths, strengths, and abrupt shift distances. Bottom: Global model (fig. S3B). Note that the y axis increments are different between the two models. Red lines denote input strength for bump jump with narrow input, which is constant for the local model and

increases with shift distances for the global model. (E) Schematics of stimulation protocol to detect the threshold input strength for bump jump in response to narrow (22.5°) input. Two 22.5° areas were sequentially stimulated. (F) Laser power required to make bump jump from the first stimulation position (1 or 2) to a fixed second stimulation position (A or B). $P = 0.102$, paired t test. (G) Input strength, estimated by normalized bump amplitude, required for bump jump from fixed first stimulation position to second stimulation position. Red dashed line denotes simulated threshold of the local model. Solid dots are trials with first stimulation at position 1; open dots are trials with first stimulation at position 2.

the local and global models (fig. S4, H and I, and supplementary text), we found that any model that exhibited the observed jumps in response to a weak 22.5° -wide input had narrow connectivity profiles (fig. S4I). All these observations were once again consistent with the local model.

In mammals, heading representations are thought to be distributed across multiple neural populations and multiple brain areas (8). In *Drosophila* as well, the compass system likely involves multiple cell types, including neurons in the protocerebral bridge (PB) (17, 23). Further, occasional changes observed in the dynamics suggest network modulation by other factors not yet known. For example, we sometimes observed sudden changes in E-PG dynamics, as when the amplitude of the sensory-evoked activity bump changed depending on whether or not the tethered fly was flying (see supplementary materials) and, occasionally, during flight [population vector average (PVA) amplitude plots in Fig. 1, G and H, Fig. 4, A and B, and fig. S1B]. Nonetheless, the E-PG population provides a

powerful physiological handle on the internal representation of heading (16): a single activity bump moving through topographically arranged neurons. The experimental approach this enabled provides one avenue for investigating which of multiple populations are key circuit components of a computation and which simply read out the results of that computation. We found that the artificial bump created by directly manipulating E-PG population activity displays natural dynamics, which indicates that these neurons are a key component of the heading circuit.

Our finding that the uniqueness of the E-PG activity bump is ensured via global competition strengthens the conclusion that this population encodes an abstract internal representation of the fly's heading direction (16). Such abstract representations permit an animal to untether its actions from the grasp of its immediate sensory environment and thereby confer flexibility in both time and behavioral use. Combining an analysis of artificially induced bump dynamics with theoretical

modeling allowed us to interrogate this recurrent circuit architecture. We found that the effective network connectivity profile was consistent with ring attractor models characterized by narrow local excitation and flat long-range inhibition. This neural circuit motif of local excitation and long-range inhibition is ubiquitous across many brain areas and across animal taxa (28–31). Such observations support the idea that common circuit motifs might be evolutionarily adapted to serve as crucial building blocks of cognitive function.

REFERENCES AND NOTES

1. R. I. Wilson, *Annu. Rev. Neurosci.* **36**, 217–241 (2013).
2. A. Borst, M. Helmstaedter, *Nat. Neurosci.* **18**, 1067–1076 (2015).
3. J. J. Knierim, K. Zhang, *Annu. Rev. Neurosci.* **35**, 267–285 (2012).
4. E. Aksay et al., *Nat. Neurosci.* **10**, 494–504 (2007).
5. H. S. Seung, *Proc. Natl. Acad. Sci. U.S.A.* **93**, 13339–13344 (1996).
6. R. Chaudhuri, I. Fiete, *Nat. Neurosci.* **19**, 394–403 (2016).
7. K. Wimmer, D. Q. Nykamp, C. Constantinidis, A. Compte, *Nat. Neurosci.* **17**, 431–439 (2014).

8. J. S. Taube, *Annu. Rev. Neurosci.* **30**, 181–207 (2007).
9. J. S. Taube, R. U. Muller, J. B. Ranck Jr., *J. Neurosci.* **10**, 420–435 (1990).
10. B. L. McNaughton, F. P. Battaglia, O. Jensen, E. I. Moser, M. B. Moser, *Nat. Rev. Neurosci.* **7**, 663–678 (2006).
11. R. Ben-Yishai, R. L. Bar-Or, H. Sompolinsky, *Proc. Natl. Acad. Sci. U.S.A.* **92**, 3844–3848 (1995).
12. W. E. Skaggs, J. J. Knierim, H. S. Kudrimoti, B. L. McNaughton, *Adv. Neural Inf. Process. Syst.* **7**, 173–180 (1995).
13. K. Zhang, *J. Neurosci.* **16**, 2112–2126 (1996).
14. X. Xie, R. H. Hahnloser, H. S. Seung, *Phys. Rev. E* **66**, 041902 (2002).
15. A. Peyrache, M. M. Lacroix, P. C. Petersen, G. Buzsáki, *Nat. Neurosci.* **18**, 569–575 (2015).
16. J. D. Seelig, V. Jayaraman, *Nature* **521**, 186–191 (2015).
17. T. Wolff, N. A. Iyer, G. M. Rubin, *J. Comp. Neurol.* **523**, 997–1037 (2015).
18. T. W. Chen *et al.*, *Nature* **499**, 295–300 (2013).
19. M. H. Dickinson, *Philos. Trans. R. Soc. London Ser. B* **354**, 903–916 (1999).
20. N. C. Klapoetke *et al.*, *Nat. Methods* **11**, 338–346 (2014).
21. M. Yoshida, M. E. Hasselmo, *J. Neurosci.* **29**, 4945–4952 (2009).
22. G. Major, D. Tank, *Curr. Opin. Neurobiol.* **14**, 675–684 (2004).
23. K. S. Kakaria, B. L. de Bivort, *Front. Behav. Neurosci.* **11**, 8 (2017).
24. S. Amari, *Biol. Cybern.* **27**, 77–87 (1977).
25. P. Song, X. J. Wang, *J. Neurosci.* **25**, 1002–1014 (2005).
26. D. Hansel, H. Sompolinsky, in *Methods in Neuronal Modeling: From Ions to Networks*, C. Koch, I. Segev, Eds. (MIT Press, 1998), pp. 499–567.
27. A. M. Turing, *Philos. Trans. R. Soc. London Ser. B* **237**, 37–72 (1952).
28. H. Ko *et al.*, *Nature* **473**, 87–91 (2011).
29. M. Weliky, K. Kandler, D. Fitzpatrick, L. C. Katz, *Neuron* **15**, 541–552 (1995).
30. H. Ozeki, I. M. Finn, E. S. Schaffer, K. D. Miller, D. Ferster, *Neuron* **62**, 578–592 (2009).
31. S. P. Mysore, A. Asadollahi, E. I. Knudsen, *J. Neurosci.* **30**, 1727–1738 (2010).

ACKNOWLEDGMENTS

We thank A. Jenett, T. Wolff, and G. Rubin for their generous sharing of the split line SS00096 before publication, and, in particular, T. Wolff for her scientific insights; B. Pfeiffer, A. Wong, D. Anderson, and G. Rubin for generously sharing codon-optimized GCaMP6f DNA before publication; C. Dan for codon-optimized GCaMP6f files; S. Romani for contributing to insightful discussions regarding bump jumps in the global model and the effect of

input width; Janelia Fly Core and, in particular, K. Hibbard and S. Coffman, for support; J. Liu for virtual reality support; D. Flickinger and V. Goncharov for microscope design support; J. Arnold for fly holder design; Vidrio for ScanImage support; S. Rowell and E. Nielson for operational support; and A. Karpova, A. Hermundstad, M. Ahrens, S. Romani, Y. Sun, and members of V.J.'s lab for useful discussions and comments on the manuscript. Supported by the Howard Hughes Medical Institute. Code for physiological data and analyses is available at http://research.janelia.org/jayaraman/KimRouaultScience2017_Downloads.

SUPPLEMENTARY MATERIALS

www.sciencemag.org/content/356/6340/849/suppl/DC1
Materials and Methods
Supplementary Text
Figs. S1 to S4
Movies S1 to S11
References (32–46)
Code for ring attractor simulation and Bayesian sampling

29 November 2016; accepted 20 April 2017
Published online 4 May 2017
10.1126/science.aal4835